THE PERFECT MIRROR HOOK? X-RAY SCATTERING MEASUREMENTS OF CRYSTALLITE CONTAMINATION IN RAPIDLY QUENCHED $(Mo_{0.6}Ru_{0.4})_{1-x}B_x$

BRIAN EMMERSON
Gonville & Caius College
Cambridge, CB2 1TA, UK

CALTECH LIGO SURF 2002
MENTOR: DR RICCARDO DESALVO
LIGO project, Caltech
Pasadena, CA 91125, USA

ABSTRACT

In a bid to reduce suspension thermal noise in the Laser Interferometer Gravitational-wave Observatory (LIGO), it has been suggested that the interferometer's mirror suspensions be replaced with metallic flex joints made from amorphous refractory metal-based alloys, namely $(Mo_{0.6}Ru_{0.4})_{1-x}B_x$. Presented here are a brief outline how these 'glassy metals' are made and the problems associated with sample inhomogeneity. To address this issue, x-ray diffraction measurements are made of specimens produced by splat cooling and the qualitative variation in composition within these samples is investigated. Angular shifts in diffraction data are discussed in the context of samples not being mounted coaxially with the x-ray detector and not found to account accurately for the observed shifts. Some attempts at quantitative analysis of phase composition are also outlined, including a technique that may allow determination of volume fractions to a precision of the order 1%.

1. INTRODUCTION

The Laser Interferometer Gravitational-Wave Observatory[1] (LIGO) is being developed to detect and study the gravitational waves predicted by Einstein's theory of general relativity. This theory anticipates the occurrence of ripples (gravitational waves) in space-time, emanating at the speed of light from massive accelerating objects. Once detected, gravitational waves will be used to provide a wealth of detailed information about their sources and a revolutionary means with which to investigate strongly gravitating bodies in the universe.

LIGO and all other Earth-based gravitational wave detectors use Michelson-Morley laser interferometers with test mass mirrors suspended at each end of the interferometer arms. Gravitational waves cause different amounts of stretch in each arm, which is in principle detectable when the laser beams are recombined. Such changes in arm length are meagre by most standards: we require to detect displacements $\sim 10^{-18}$m. Consequently, a major driving force behind LIGO engineering is the reduction of noise. For frequencies in the range 10-200Hz, noise is predominantly due to off-resonance, thermally induced vibrations of the test masses and their suspensions. The gravitational wave frequencies of certain key sources [an inspiralling black hole-black hole system (each 10 to 1000 solar masses) has an innermost stable circular orbit (ISCO) frequency in the range 4-400Hz] means that reduction of this effect is essential.

In the presently operational version of LIGO, mirrors are suspended by piano wire slung around their circumference – a method to be improved when the interferometer is upgraded to Advanced LIGO in 2007. Fused silica fibres – attached to the mirrors via silicate bonding – are the proposed upgrade (chosen mainly because of the high intrinsic Q-factor of fused silica), though they are susceptible to hydroxyl attack and the load to which the fibres can be subjected is limited (<1GPa) by reliability considerations to well below that which metals can support. An alternative solution is the use of metallic flex joints from which the mirrors can be hung in the more familiar 'wall-hook' type of arrangement. Development of these suspensions was considered several years ago but abandoned because of the poorer intrinsic Q factor of metals and much larger research effort concerned with fused silica at the time. Recently interest has been rekindled in developing flex joints incorporating amorphous (glassy) refractory metal-based alloys, which have a relatively high intrinsic Q factor. Although this Q factor is smaller than that of fused silica, it is possible to make the *overall* flex joint's Q equal to or even higher than that of a fused silica suspension, simply by making its active part thinner (a luxury afforded by a higher yield point and fracture toughness), providing a suspension far more resistant to defects and immune to hydroxyl attack.

A programme of research[2,3] is underway to determine the material properties of amorphous $(Mo_{0.6}Ru_{0.4})_{1-x}B_x$ for x = 0.14 to 0.24 and it is with this research that this paper is concerned. Unfortunately, the rapid cooling technique (§3.2) we employ to freeze alloys into a metastable glassy state (as opposed to the stable crystalline state) does not produce samples that are homogeneously amorphous. In order to locate regions of samples with low crystallite contamination, we study the diffraction patterns produced when samples are irradiated with soft x-rays. Using the fact that amorphous materials have diffraction patterns very different to those produced by a crystalline phase of the same material, we are able to make some inferences about a sample's composition. These measurements form the main focus of this paper.

2. BACKGROUND

2.1 Loss mechanisms and choice of materials

Dissipation of suspension oscillation energy from crystalline materials results in part from lattice dislocations 'jumping' out of phase with a varying applied stress, a mechanism that has a far smaller effect in amorphous materials (which lack a periodic lattice of atoms). However, this does not mean that all amorphous metals are suitable for the construction of LIGO mirror suspensions: when varying stresses are applied to ferrometallic-based alloys, hydrogen absorbed into the matrix jumps from compressed regions to stretched ones, dissipating energy in the process (we have fluctuation-dissipation governed behaviour). This problem is overcome by the use of refractory metal-based alloys, in which hydrogen absorption is negligible. When amorphous, these materials have critical defects >10μm in size (whereas those for fused silica are

submicron-scale), meaning that in the absence of visible flaws they can be reliably loaded close to their breaking point (allowing the use of thinner flex joints and reducing the amount of energy stored in the flex joint) – a considerable advantage when each mirror costs a sizeable fraction of $1M. Unless unknown loss mechanisms are observed, the use of alloys such as $(Mo_{0.6}Ru_{0.4})_{1-x}B_x$ should provide suspension Q factors competitive with fused silica.

2.2 Glassy metals: principles of production

In order to freeze a molten metal into an amorphous state[4], it is necessary to cool it without allowing crystal nucleation. This can be achieved by rapid rates ($\sim 10^6 Ks^{-1}$) of cooling but the process is greatly assisted by using two species of atoms to "frustrate" the crystal formation process by chemical disorder. The addition of a third species that is appreciably different in atomic size further frustrates crystal formation. In $(Mo_{0.6}Ru_{0.4})_{1-x}B_x$, the principal rôle of boron is just this: filling the interstices present in the disordered molten structure and hindering establishment of a periodic structure. The 'splat quenching' method we employ (§3.2) to cause rapid cooling is only partially successful in producing amorphous phases. Crystal formation in parts of samples increases fragility and results in undesirable non-uniform distributions of stress when the sample is placed under tension, lowering the loads it can support.

2.3 Addressing sample inhomogeneity

Before a rapidly quenched sample of $(Mo_{0.6}Ru_{0.4})_{1-x}B_x$ can be subjected to tests to determine optimal specifications for its use in a flex joint, we need to ensure we are indeed testing a truly amorphous specimen. For the samples to be available for other tests and actual use, the procedure employed to do this must be non-destructive, ruling out techniques like transmission electron microscopy – it requires sample thicknesses of at most a few hundred nanometres: far less than the minimum thickness of material (~10μm) needed for a suspension. Instead, we use diffraction of x-rays.

X-ray diffraction by crystalline materials is described by the well-known Bragg equation, which accounts for sharp peaks (see fig. 2.1) in the diffracted intensity whenever the total incident beam deflection $2q$ matches the condition $2a\sin q = nl$. (a is the spacing between a set of interatomic planes and nl is an integral number of x-ray wavelengths l – further details are provided in the appendix, §A.1.) The situation with amorphous materials is more complicated: interatomic distance is basically maintained and the atomic bond is the same, but the periodicity is disrupted over distances longer than 2 or 3 atomic distances. In contrast to the sharp peaks produced by crystalline materials, the much larger variation in atomic separation found in amorphous samples produces patterns with broad, smooth peaks (fig. 2.2), corresponding to scattering by first, second and higher-order neighbour pairings. A detailed model of the how this pattern of diffracted intensity arises from a one-dimensional amorphous material can be found in [5].

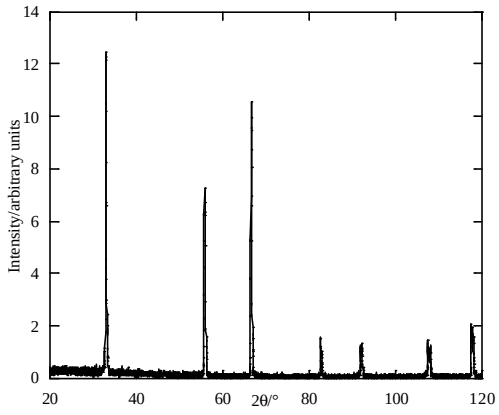

fig. 2.1
Powder diffraction pattern from polycrystalline silicon. Diffracted intensity (in arbitrary units) is plotted against $2?$, the total beam deflection.

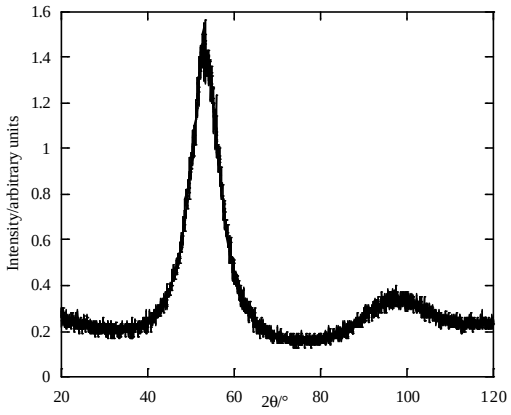

fig. 2.2
Diffraction pattern from the industrially produced iron-based amorphous metal, Metglas. Compare the broad, smooth peaks here with the narrow, sharp ones of fig. 2.1.

A sample of mixed phase produces a corresponding 'mixed' diffraction pattern, with a

diffracted intensity governed by Vainshtein's law, which states that "within identical regions of reciprocal space, the diffracted intensity from a material will be independent of its state of order." This sum rule dictates that integrated diffracted intensities from different phases should be equal, provided the range of integration is sufficiently larger than the width of a glassy peak. Some of our tried, tested and rejected techniques for determining phase composition are discussed in §4.4.

3. METHODS

3.1 Alloy preparation

Initial alloying of $(Mo_{0.6}Ru_{0.4})_{1-x}B_x$ is done under argon in a mini arc melter by melting and remelting appropriate quantities of the constituent elements until a homogeneous tablet forms. Repeated casting under suction is then used to convert the tablets into a form that can easily be broken and remelted into 135-140mg (3mm diameter) spherical beads – surface tension is sufficient to draw the molten alloy into this shape. Rapid quenching of these samples is then performed in the twin-piston apparatus (splat quencher) described below.

fig. 3.1a **fig. 3.1b**

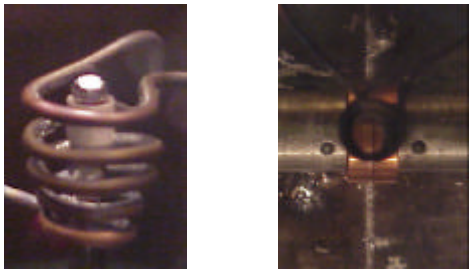

A bead in the pre-levitation sample holder is shown in **fig. 3.1a**. Once current is flowing, an energy density that increases with distance down the coil (on-axis energy density in a single coil scales inversely with the square of its radius) provides an upward force to balance the effects of gravity. **fig. 3.1b** shows splat quenching at the instant of piston collision, viewed through the levitation coil. Molten alloy is seen being squeezed from between the pistons.

3.2 Splat quenching

The rapid rates of cooling described in §2.2 are achieved by 'splatting' the molten beads between two copper anvils. To do this, a radio-frequency (RF) current is passed through a conical coil – in vacuo – with the sample at its centre (fig. 3.1a). The decrease in magnetic energy density with increasing coil radius produces an upward force on the bead sufficient to balance the effects of gravity; whilst at the coil's top a single counter-wound turn restrains the bead from falling out of the cone. Induced RF eddy currents resistively heat the levitating bead until molten, before termination of the coil current causes the sample to fall and intersect a laser beam trigger for the pistons, which advance at high speed to spat the molten sample between them. Fig. 3.1b shows a sample in the process of being splatted.

Care must be taken to retract the pre-levitation sample holder as smoothly as possible: any jerks start oscillations that grow with time. Our choice of mass mentioned above (§3.1) was made as a compromise between the desirable fast cooling rates associated with small spheres and the undesirably large oscillations these spheres can exhibit upon jerky removal of the bead holder once levitation is achievable – large oscillations can mean that a bead falls out of the sample holder before it becomes molten or that it fails to cut the laser beam used to trigger the pistons.

3.3 X-ray diffraction (XRD)

The rapidly quenched foils (fig. 3.2) are mounted on the axis of an argon-ethane filled, curved-blade ionising event detector designed to detect x-rays over 120° of beam deflection. Monochromatic Co $K\alpha_1$ (6.93keV) radiation – which has a characteristic attenuation length ~1μm for molybdenum – is used to irradiate the samples.

fig. 3.2
Typical rapidly quenched samples, such as the one above, are in the form of foils roughly 20mm in diameter and between 40 and 60μm thick. A halo of radial crystalline 'fingers' forms around the circumference as a result of the slower cooling that occurs there. The composition of these foils is discussed further in §4.3.

Signals are recorded at 1024 positions along the length of the detector and an automated interpolation technique gives readings from 4096 channels. Channel number is converted to the conventional deflection angle $2q$ using the powder diffraction pattern for polycrystalline

silicon (fig. 2.1), produced by the same apparatus.

To investigate phase variation within samples, it is necessary to accurately locate the point where they are irradiated by the x-ray beam and this was initially done using fluorescent paper mounted on the same glass slides used to support the samples. The position of the bright spot produced was used to establish where the same beam would hit the sample, with subsequent locations determined by recording slide displacements. [Ideally, such displacements would be made mechanically using a translation stage but, owing to present problems with monochromator alignment, the department owning the machine are understandably reluctant for such a modification to be made at this time.] In order to investigate variations across a sample, the x-ray spot size must be fairly small, which means that irradiating a whole sample is time consuming. As an automated mechanical means for moving samples would allow whole splats to be tested without monitoring, steps have been made towards setting up a computer-controlled stage.

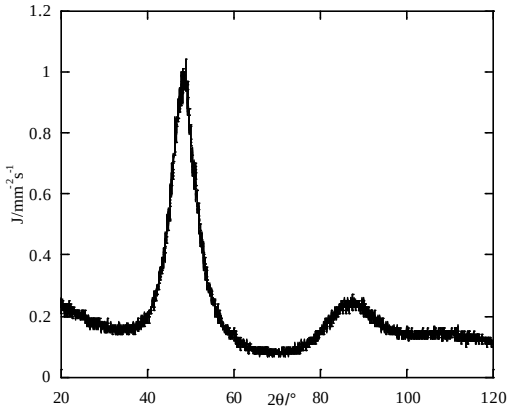

fig. 4.1
X-ray diffraction pattern from an amorphous region of $(Mo_{0.6}Ru_{0.4})_{0.83}B_{0.17}$. [This data was taken from region E of fig. 4.7.]

4. Discussion of Results

4.1 General results

Investigation of crystalline and glassy $(Mo_{0.6}Ru_{0.4})_{0.83}B_{0.17}$ (x = 0.17) yielded the expected distinct diffraction patterns: glassy $(Mo_{0.6}Ru_{0.4})_{0.83}B_{0.17}$ (fig. 4.1) gives a smooth, broad first nearest neighbour diffraction peak with an angular ($2q$) full width at half maximum (AFWHM) of approximately 8.5°, whereas the crystalline form (fig. 4.2) produces low-angle peaks with AFWHM ~ 0.4° (these estimates are obtained by fitting a Gaussian curve to each peak). Some sample regions yielded intermediate patterns and these are discussed further in §4.3. In all of the figures below, flux ($J/mm^{-2}s^{-1}$) is plotted against beam deflection ($2q$): a flux value corresponds to the raw event count divided by the area of the final x-ray aperture and the time of exposure.

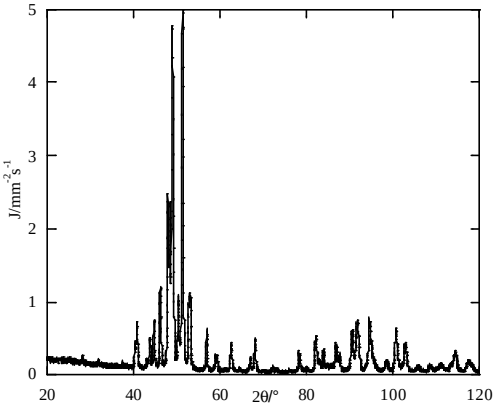

fig. 4.2
X-ray diffraction pattern from crystalline $(Mo_{0.6}Ru_{0.4})_{0.83}B_{0.17}$. Compare the 'forest' of peaks produced here with the few from polycrystalline silicon in fig. 2.1. Many more peaks arise here due to the presence of more than one element and atomic spacing.

4.2 Observed shifts in data

Because some of the data analysis techniques employed (§4.4) involve comparison between different sets of data, it is reasonable to ask if there exist any observable systematic discrepancies in data taken from different compositions and on different dates. The short answer to this question is yes, and the findings are outlined below. Investigations of data shifts were made using crystalline samples because of their narrower, more numerous and easily locatable peaks.

4.2.1 Data pattern shifts between dates

One initially surprising distinction between sets of data taken from the same sample but recorded on different days was a difference in peak position dq that increased nonlinearly with diffraction angle; an effect not explained by, say, a poorly calibrated set of data. A possible cause of such a shift is a difference in temperature producing a uniform change in interplanar spacing a, which (from differentiation of the Bragg equation) should be related to an angular

shift via $dq = -(da/a)\tan q$. Fig 4.3 and the following argument show that this explanation cannot be correct.

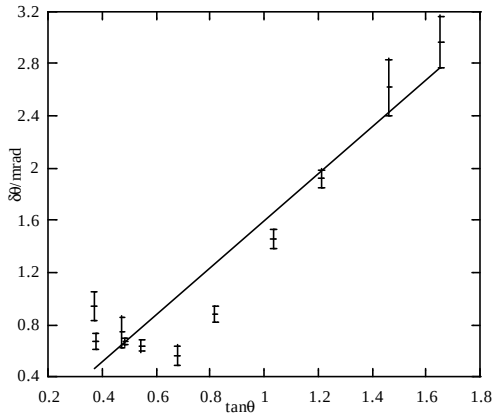

fig. 4.3
Graph showing the poor fit of the data shifts to the law $dq = -(da/a)\tan q$.

The linear expansion coefficient of $(Mo_{0.6}Ru_{0.4})_{0.83}B_{0.17}$ can be reasonably approximated (for the purposes of an order of magnitude calculation) by that of another metal such as steel ($\sim 10^{-5} K^{-1}$). When this is compared with the fractional change in lattice parameter obtained from the linear fit shown in fig. 4.3, it corresponds to a difference in temperature ~200K, which the author believes he probably would have noticed. Even fitting a line to the data at smaller values of $\tan q$ does not provide an estimate that is much more sensible. Furthermore, the distribution of points is not consistent with Gaussian errors in both cases.

An alternative explanation for the observed shifts is provided by fig. 4.4, which illustrates the shift introduced when a sample is not mounted concentrically with the curved detector. However, fig. 4.5 shows that agreement with this explanation is also poor.

Both fits used in fig. 4.5's data are consistent with displacements of the sample ~1mm (the radius of curvature of the detector is 250mm), which is plausible but the inadequate match of data with the rule derived in fig. 4.4 suggests that this is not the only reason for the observed shifts, if it does make a contribution at all. What has been shown, however, is that angular changes such as those observed are comparable with the effects of moving the sample off-axis by a millimetre or so. For future measurements, care must be taken in mounting the sample at the detector's centre.

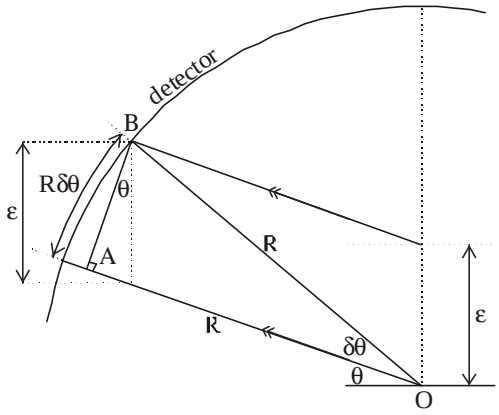

fig. 4.4
From above, we see that length $AB = e\cos q \sim R\,dq$ (where R is the radius of the detector), with true equality in the limit $dq \sim dq$. It follows that the apparent angular displacement introduced by a normal displacement e from the detector's centre O is $dq = (e/R)\cos q$.

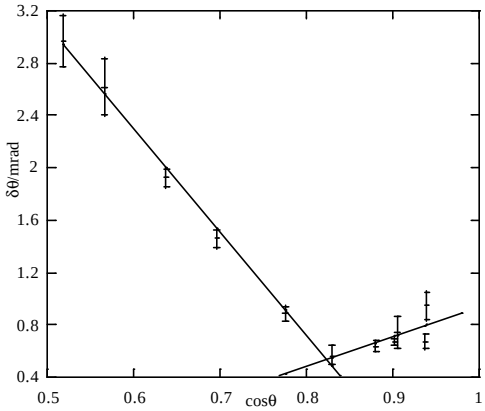

fig. 4.5
Another poor fit of the angular shift data to a suggested model. Here two regions have been identified where the data may fit the law $dq = (e/R)\cos q$, with the assumption that other (unexplained) effects dominate in the other half of the $\cos q$ values. Although the calculated values for e are sensible, the data does not support the conjecture that sample displacement is the *only* reason for the shifts observed.

4.2.2 Data shifts between compositions

From comparison of the diffraction patterns from different compositions (x = 0.17, 0.20, 0.21) of crystalline $(Mo_{0.6}Ru_{0.4})_{1-x}B_x$, it was found that each pattern contained the same number of peaks in roughly the same position. This is not surprising: the samples contain the same set of chemical bonds, each producing a peak at a given point in the diffraction pattern. Again, shifts in angle could be due to offsets in the sample position, though the agreement is as

inconclusive as that in §4.2.1. Closer inspection of a narrow angular range (fig. 4.6) reveals that the peaks have the same underlying shape, which is most likely explained by the distribution of atomic separations within a given composition being the same across the three compositions tested.

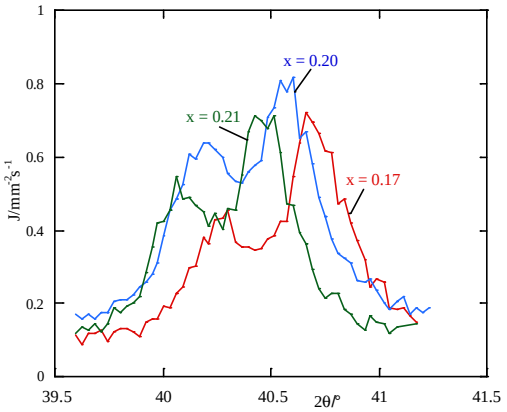

fig. 4.6
Peaks in the diffraction patterns of $(Mo_{0.6}Ru_{0.4})_{1-x}B_x$ for x = 0.17, 0.20, 0,21. Despite shifts ~0.1° in their position, this figure clearly shows the similar underlying peak structure.

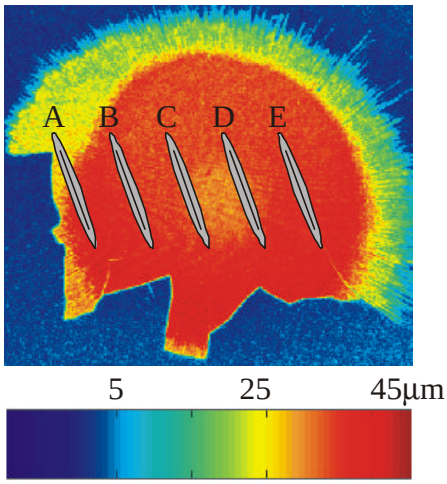

fig. 4.7
X-ray microdensitometry image of $(Mo_{0.6}Ru_{0.4})_{0.83}B_{0.17}$. An indication of the thickness of material present is given in the scale along the bottom of the figure, though the principal purpose of these images is for the detection of defects –see [6]. Regions of apparently thin material around the circumference are due to the area there being made up of many fine fingers of crystalline material. A-E indicate five different areas investigated for this particular splat, where each region shows the approximate area irradiated with x-rays, set by the height and width of the final aperture in the x-ray beam. Variations in the resulting scans are discussed in the text. Easy breaking of a sample (as is seen here) is typical of a splat with mixed phase composition: glassy regions in samples tend to be more flexible as well as resistant to the propagation of cracks, meaning that fracture end points tend to signify a change in phase from crystalline to quasi-amorphous.

4.3 Composition variations within samples

Fig. 4.7 shows a microdensitometry image of a broken splat, obtained by irradiating a sample of $(Mo_{0.6}Ru_{0.4})_{0.83}B_{0.17}$ with medical x-rays and scanning the negative into MATLAB (further details about the production of these images can be found in [6]).

From x-ray diffraction measurements of this splat, qualitative variation in the proportions of crystalline and amorphous material is noticeable. Although it might be expected that the thinnest areas of material would have the greatest degree of 'glassicity' owing to a faster rate of cooling, the patterns from regions A-E reveal that this is not necessarily the case.

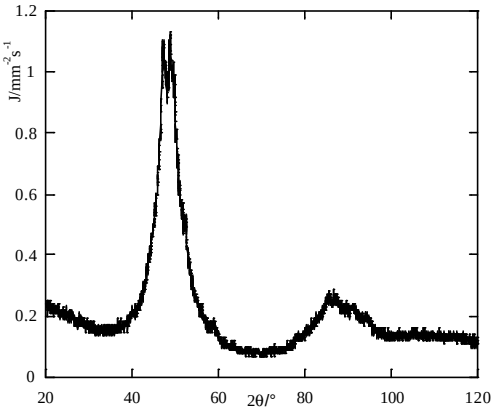

fig. 4.8a
X-ray diffraction pattern from region C of fig. 4.7.

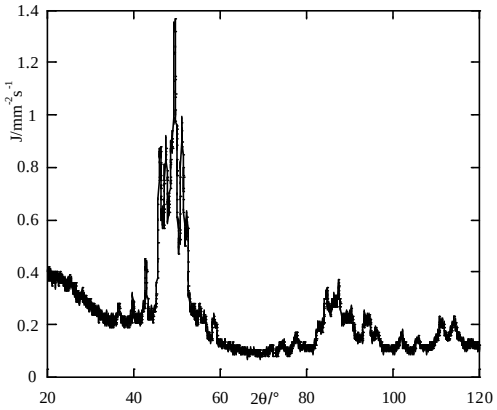

fig. 4.8b
X-ray diffraction pattern from region A of fig. 4.7.

For example, if fig. 4.8a (from region C) is compared with fig. 4.1 (from region E), it can be seen that region C has a noticeable crystalline contribution to its diffraction pattern (with narrower peaks seen sticking out above the mainly glassy data), whereas section E does not.

This is despite section C being thinner than section E. For the remaining areas of fig. 4.7, region D contains a near-identical crystalline character to region C, with region B having a slightly smaller such contribution. The diffraction pattern from region A (fig 4.8b) is dominated by a crystallite contribution with a larger amount of 'noise' at lower angles, the former being chiefly due to this region incorporating some of the crystalline halo and the latter to a small contribution from the glass slide on which the sample is mounted with double-sided tape.

In order to check whether the variation in composition described above is a common feature of all splats of $(Mo_{0.6}Ru_{0.4})_{0.83}B_{0.17}$, other samples were investigated in a similar manner, only with a smaller aperture size (to allow investigation of smaller areas). Of two further splats investigated, one exhibited similar characteristics to those listed above, whereas the other produced predominantly amorphous patterns with little visible variation between regions within the crystalline halo. Microdensitometry of these samples shows the splat with the more uniform composition to be predominantly wedge-shaped, without the thinner centre found in the ones with more varied composition. This suggests that there may be some correlation between the uniformity of a splat and its phase composition, though further investigation is needed to confirm this. It is worth bearing this in mind, since sample areas measuring ~3mm x 6mm are needed to construct flex joints. Preliminary investigations of such sample "strips" suggest that it is indeed possible to produce glassy samples of this size. Ultimately, to perform a more precise analysis of phase composition, we need to test small splat areas (by reducing the final aperture size on the x-ray tube) and take many samples. However, this is extremely time consuming without the use of an accurate automated positioner.

4.4 Attempts at quantitative analysis

In attempts to get some quantitative idea of sample composition, several methods of manipulating data were attempted, of which three are presented here. The first of these involves locating peaks in the diffraction pattern of a crystalline sample using Gaussian fits and a curve fitting function in Kaleidagraph. Recorded peak positions are then used as the starting points in a search for crystalline peaks in quasi-glassy patterns by forcing the curve-fitting algorithm to find curves of a fixed width, the idea being that the area under these peaks be evaluated and used to estimate phase volume fractions. This method proved unsuccessful because of the curve finding function's inability to reliably locate peaks that were clearly visible by eye, the main problem being the 'confusion' (Poissonian) statistical scatter causes the algorithm. A longer exposure of the sample would reduce this scatter, but because the fractional intensity variation varies undesirably with the inverse square root of the exposure time, relatively long exposures are needed to achieve this effect to the required extent and the technique was not pursued further because of this.

It is possible to manipulate the distinct difference in the peak widths produced by different phases and this forms the basis for the second method discussed here. Smoothing data over a range larger than a typical crystalline peak width but smaller than that of a typical glassy one has the effect of preferentially flattening out crystalline features but leaving glassy ones unscathed. Subtraction of the smoothed curve from the raw data removes the glassy features (almost) entirely but leaves the crystalline ones, albeit somewhat diminished and deformed. This has the effect of making sharp features more apparent to the eye, but it is difficult to estimate how much of each one has been subtracted, making accurate phase estimations complicated.

The final method discussed here encompasses aspects of both above-described ones. It involves smoothing data from a "purely glassy" sample over a range greater than a typical crystalline width but far less than a glassy width. The effect is to produce a curve like that in fig. 4.9. If the data in this figure is taken to represent the pattern from a truly amorphous sample, it can be fractionally subtracted from a real quasi-glassy set of data to (in principle) leave only the crystalline contribution to the diffracted intensity. The data to be tested are normalised to ensure the integrated intensity is numerically equal to that of the smoothed 'reference' data. This must be done between the same angular limits, for the reasons outlined below.

With scattering centres of finite extent there exists a fall-off in intensity with increasing beam deflection (perfectly point-like centres would produce an intensity uniform in $2q$ if irradiated with unpolarised radiation) and this affects the

diffraction patterns produced by reducing the intensity diffracted to higher angles. Furthermore, x-rays received at the sample are polarised by their dipole interaction with the atoms of the graphite monochromator, meaning that the scattered intensity by a single centre will not be isotropic, even in the limit that the scattering centres are perfect *d*-functions. It follows that whenever a comparison is made between diffracted intensities from two different samples, it must be done over the same angular range to ensure these phenomena affect both patterns equally and allow any rescaling of areas to be as accurate as possible.

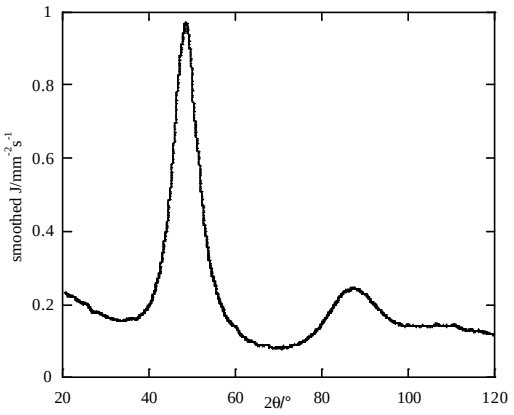

fig. 4.9
Smoothed glassy data (from section E of fig. 4.7). The pattern presented here is that from fig. 4.1, with each point averaged over the surrounding 30 flux values. This is equivalent to smoothing over a range of $2q$ of almost 0.9°.

Renormalisation of areas to allow inter-data comparison is based on the assumption that equal integrated intensities are produced by samples exposed for equal lengths of time using the same beam intensity and aperture areas. This assumption is validated by the observation that, even before nornalisation, both glassy and semicrystalline regions of the same splat (fig. 4.7), exposed for equal periods to the same x-ray intensities, produced identical integrated fluxes (between 20° and 120°) within one or two percent.

Once a set of data has been normalised to make its area (between 20° and 120°) equal to that of the smoothed pattern of fig. 4.9, the diffraction pattern from a purely crystalline sample of the same material is consulted. In the crystalline pattern there exist ranges of $2q$ (e.g. from $2q$ = 73.5° to 75.5° when x = 0.17) in which there are no Bragg peaks: no peaks will be produced in these regions by crystallite contaminations in a mainly glassy sample either. Whether a sample is glassy or not, subtraction of the smoothed "purely glassy" data from the scaled data under question should result in an integral that is zero over the angular ranges containing no crystalline peaks. In scaling the smoothed data by some coefficient C<1 before subtracting it from the data being analysed, it is always possible to arrange for the resulting integral to be zero. Using Vainshtein's law we identify C as the volume fraction of glassy material in the sample being tested, with the remaining fraction of material being crystalline.

Figs 4.10a and 4.10b illustrate the subtraction process. By adjusting the value of C to arrange for zero integrated flux over a region of $2q$ not containing any crystalline peaks, we can estimate the volume fraction of amorphous material. Using the data in fig. 4.8a, we deduce that material in region C of fig. 4.7 is 96.6±1.0% amorphous by volume. The error in the volume fraction of amorphous material is estimated using the fact that the expression for C is found by solving

$$\int_a^b \{J_f(x) - CJ_g(x)\}dx = 0,$$

where $x = 2q$. J_f is the flux from the quasi-glassy sample, J_g is that for the perfectly glassy data (fig. 4.9) and the range of integration $x = [a,b]$ contains no crystalline peaks. Hence

$$C = \frac{\int_a^b J_f(x)dx}{\int_a^b J_g(x)dx}.$$

Equivalently,

$$C = \frac{< J_f(x) >}{< J_g(x) >},$$

provided the range over which the average is taken is $[a,b]$. This last equation can also be used to calculate C, but more importantly it gives an estimate of σ_C from the standard errors in the averages of J_f and J_g, giving some indication of the way in which data are scattered in these regions. The precision of the technique could be improved by increasing the range $[a,b]$ (equivalent to increasing the number of values over which the averages are calculated). However, owing to the forest of peaks (fig. 4.2), much larger ranges not containing any notable Bragg peaks are hard to come by. The other way to improve the statistical precision is to take data

for longer time and gain with $1/\sqrt{n}$. Although one can indefinitely reduce the statistical sensitivity, the estimation error in the crystallite fraction is limited by systematics, mainly background scattering. We somewhat arbitrarily estimated the systematic error to 1%. Lower systematic errors can be obtained by carefully controlling the x-ray spot (to avoid scatter from the support structure that would spoil the subtraction process).

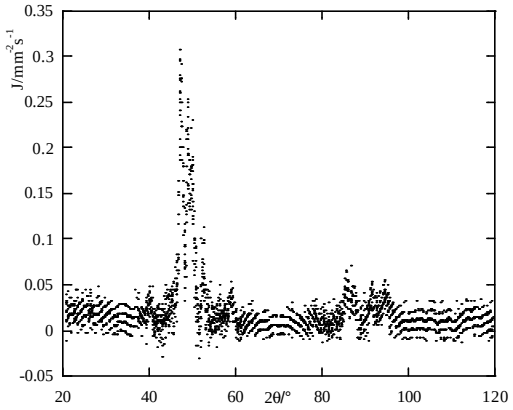

fig. 4.10a
Data from fig. 4.8a with a scaled amount of the ("pure glassy") data in fig. 4.9 removed from it with the intention of making the integrated flux zero between $2q$ = 73.5° and 75.5°. Here too little (C = 0.90) of the glassy data is subtracted and the resulting integral is positive. The texture seen in the digital data is due to counting and round-off noise.

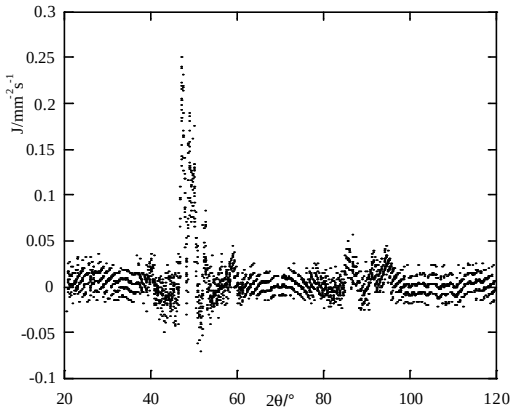

fig. 4.10b
Here the correct amount of glassy data is removed to leave zero integrated flux between $2q$ = 73.5° and 75.5°, The value of C required to do this is 0.966±0.010[±0.01], where the quantity in square brackets is an estimate of the systematic error.

Any technique used to extract phase volume fractions from x-ray diffraction data may be calibrated against a technique like transmission electron microscopy (TEM), to check its reliability. We presently plan to x-ray every single flex joint before use because this technique is at present the only non-destructive one capable of guaranteeing absence of crystallites in the glass. It may be that the fastest way to determine how suitable (free from crystallites) a particular sample region is for use in a flex joint will be to subtract as much of the glassy background as possible – to increase the visibility of crystallite traces – and then simply inspect diffraction data 'by eye'. This is an improvement on the simple 'eyeballing' technique used in [7].

From the operational point of view of making flex joints, by comparing the results of the scattering patterns with physical tests (bending limits and hardness of neighbouring parts cut from the flex joint) it may not even be necessary to measure the crystallite content with x-ray scattering each time, if correlations between visible features of x-ray diffraction patterns and other physical tests turn out to be reliable enough.

4.5 Scanning electron micrograph (SEM) analysis

Scanning electron microscopy was performed as a separate and additional test on our samples. By analysing the x-rays emitted from a sample placed in the electron beam of an SEM, it is possible to determine which heavy elements are present in the area of sample under study. This analysis was carried out with limited success for molybdenum and ruthenium (boron has too low an atomic number for the x-rays it emits to be recorded by the SEM's x-ray detector). Although the method used was not accurate enough to determine relative concentrations, initial results from areas measuring ~500µm x 500µm were encouraging, with no impurities detected above background noise. However, in one sample there did exist a series of regions measuring ~20µm x 10µm that contained significant spectral contributions from iron, chromium and silicon. A likely source is the mini arc melter used to alloy the samples, which is used by a variety of research groups within the lab. Whilst these regions are not large or widespread enough to be of immediate concern, and contamination may be confined to the splat surface, which is in any case polished away, the risk of such contamination is clearly something that needs to be considered in the future. These results stress the importance of cleaning the Mini Arc Melter before each use.

5. Conclusions and suggestions

In this paper concerning the investigation of crystallite contamination in rapidly quenched $(Mo_{0.6}Ru_{0.4})_{1-x}B_x$ alloys using x-ray diffraction, the principal findings are as follows:

1. the twin-piston apparatus employed to rapidly quench molten balls of $(Mo_{0.6}Ru_{0.4})_{1-x}B_x$ is producing some samples with regions containing very little evidence of crystallite contamination in their x-ray diffraction pattern;
2. thinner regions of foils (splats) thus produced are not necessarily those containing the least crystallite content – preliminary tests suggest that the distribution of thickness in the splats as a whole has some bearing on the size of amorphous areas produced, though further results are required to confirm this;
3. to be able to investigate areas of sample in finer detail and obtain better estimates of the location of non fully amorphous regions, investigation with a smaller beam spot size is needed, combined with the ability to make more precise movements of the samples in the x-ray beam;
4. although the size of angular shifts observed in some of the recorded diffraction patterns can be explained in terms of a poorly positioned sample, this does not appear to be the only reason for their occurrence;
5. a quantitative means for obtaining volume fractions of glassy and crystalline material was achieved, allowing us to determine apparent crystallite contamination volume fractions to a precision of the order 1%;
6. some $(Mo_{0.6}Ru_{0.4})_{1-x}B_x$ samples have acquired small amounts of contamination in the process of production – this does not appear to be a significant problem now because the contaminated regions are small and sparse, but may need addressing in the future.

A further problem may arise when cutting samples into strips to test properties such as the Young's modulus: samples are cut using electrical discharge machining (EDM), which partially melts in the immediate vicinity of the cut. It is difficult to make x-ray diffraction measurements of just a sample edge, but it is feasible by supporting the cut sample on top of another, fully glassy sample of the same composition. In this case the background will not contribute any crystallite peaks to the diffraction pattern. We will be able to efficiently subtract any glassy component, even if this means losing the quantitative aspect, and any residual crystallites on the cut edge will be apparent. It will be worth investigating how much EDM causes crystallisation of significant portions of the cut strips: since we will use electropolishing to remove the crystallised fraction, we will need x-ray scattering to verify the effectiveness of this technique and to tell us how much of the sample needs removing.

6. REFERENCES

[1] Abramovici, A. et al., *LIGO: The Laser Interferometer Gravitational-Wave Observatory*, Science **256** pp325-333, 1992;
[2] see LIGO SURF Project by Tirelli, S. and Wang, C., *Stress-strain behaviour of MoRuB glassy metals*, LIGO DCC ref. G020441-00-R, 2002;
[3] see LIGO SURF projects by Simoni, B., *Phase transition heat in MoRuB*, LIGO DCC ref. G020439-00-R, 2002; Mantovani, M., *Hardness and elasticity measurements*, LIGO DCC ref. G020440-00-R, 2002; Hall, M. [title and LIGO DCC ref. to be confirmed], 2002;
[4] see Johnson, W. L., *Bulk glass-forming metallic alloys: science and technology*, MRS Bulletin, p42, October 1999 for further details;
[5] Fultz, B., *Transmission electron microscopy and diffractometry of materials*, (Springer, 2001);
[6] see LIGO SURF projects by Kort, E., X-ray microdensitometry of amorphous MoRuB for LIGO flex joint mirror suspensions, [LIGO DCC ref. T020157-00-D], 2002;
[7] Johnson, W. L. and Williams, A. R., Structure and properties of transition-metal–metalloid glasses based on refractory metals, Phys. Rev. B, **20**, 1640, 1979.

7. ACKNOWLEDGEMENTS

This project would not have been possible without the help of the following people. I'd like to thank Dr Riccardo DeSalvo for finding the time to supervise *another* summer student (me), for his continual support and infectious enthusiasm and, most notably, the occasional Italian idiom that clearly suffered terribly at the hands of translation. Thanks also to all those working with Ric on glassy metals this summer, whose company made work a really fun place to be. The faculty of Caltech's Keck Materials lab were all a source of much appreciated help and advice and thanks go to Prof. Brent Fultz and Jason Graetz for the use of the x-ray diffraction equipment. Finally, I'd like to thank all at LIGO and the SURF office at Caltech for making this summer such an enjoyable experience inside and outside the laboratory.

A. APPENDIX

A.1 The geometry of diffraction

Fig. A.1 shows that the relevant angle involved in the diffraction process is the total beam deflection $2q$ by a given crystal, which is independent of sample orientation.

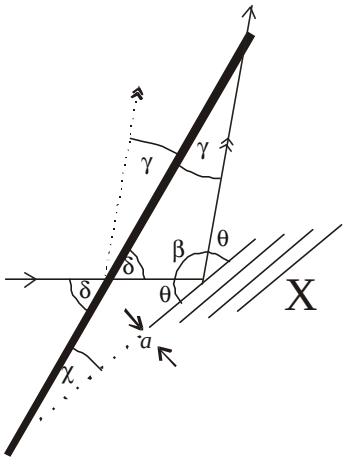

fig A.1
The geometry of diffraction. A crystal X with planes of spacing a inclined at angle c to the sample surface is irradiated by x-rays. The total deflection of the incident beam $g + d = \pi - b = 2q$ is independent of the angle d at which the radiation strikes the sample. All crystals with this orientation will produce a total deflection of $2q$, where $2a\sin = n\lambda$.